Transport- and diffusion-based optical tomography in small domains: a comparative study

Kui Ren,[1,*] Guillaume Bal,[1] and Andreas H. Hielscher[2]

[1]Department of Applied Physics and Applied Mathematics, Columbia University, New York, New York 10027 USA
[2]Departments of Biomedical Engineering and Radiology, Columbia University, New York, New York 10027 USA

*Corresponding author: kr2002@columbia.edu

Received 8 May 2007; accepted 3 July 2007;
posted 25 July 2007 (Doc. ID 82825); published 11 September 2007

We compare reconstructions based on the radiative transport and diffusion equations in optical tomography for media of small sizes. While it is well known that the diffusion approximation is less accurate to describe light propagation in such media, it has not yet been shown how this inaccuracy affects the images obtained with model-based iterative image reconstructions schemes. Using synthetic nondifferential data we calculate the error in the reconstructed images of optical properties as functions of source modulation frequency, noise level in measurement, and diffusion extrapolation length. We observe that the differences between diffusion and transport reconstructions are large when high modulation frequencies and noise-free data are used in the reconstructions. When the noise in data reaches a certain level, approximately 12% in our simulations, the differences between diffusion- and transport-based reconstructions become almost indistinguishable. Given that state-of-the-art optical imaging systems operate at much lower noise levels, the benefits of transport-based reconstructions of small imaging domains can be realized with most of the currently available systems. However, transport-based reconstructions are considerably slower than diffusion-based reconstructions.

OCIS codes: 170.0170, 170.3010, 170.3660, 170.3880, 170.6960, 170.7050.

1. Introduction

Diffuse optical tomography (DOT) is an emerging biomedical imaging technique where visible and near-infrared light is used to probe the absorption and scattering properties of biological tissues [1–13]. Applications of this technique include, for example, brain [4,14,15], breast [6,16–19], and joint imaging [20–24]. So far, most of the imaging algorithms in DOT are model based, in the sense that a model for near-infrared light propagation in tissues must be provided. It is generally believed that the propagation of near-infrared light in tissues is best modeled by the radiative transport equation (RTE), which is formulated in phase space, i.e., the space of positions and directions and thus computationally very expensive. To lower computational cost, it is preferable in many applications to replace the transport equation by its diffusion approximation, which models the spatial density of photons.

The application of the diffusion equation in optical tomography, however, has its limitations. Essentially, the derivation of the diffusion equation from the RTE is only valid when the underlying tissues are highly scattering and weakly absorbing. The diffusion approximation is not accurate enough to model light propagation in regions with small or vanishing scattering coefficients, such as the cerebrospinal fluid layers in the human head. In this case, one either has to generalize the classical diffusion equation [25], couple diffusion with transport equations [26–28], or solve the RTE directly [29–33]. Another situation where diffusion approximation is not accurate enought, and somewhat related to the previous one, is in modeling light propagation in media of small volumes. Examples are imaging of rheumatoid arthritis in finger joints [20–24] or imaging of small animals [34–36]. In these cases, because of the small optical distance

0003-6935/07/276669-11$15.00/0

between sources and detectors, the diffusion approximation is not accurate enough to approximate the "transport" behavior of photons.

The objective of this paper is precisely to compare reconstructions that rely on the diffusion equation with those based on the RTE in circumstances where a diffusion equation does not approximate the transport equation very well. Focusing on the problem of small domains, we show that considerable differences between reconstructions with transport and diffusion models exist. In general the diffusion-based reconstructions have a larger error in the values of absolute optical properties. However, diffusion-based reconstructions are considerably faster and often at least locate the heterogeneity correctly.

The remainder of the paper is structured as follows. In Section 2 we briefly recall basic facts about the RTE and its diffusion approximation. We then present in Section 3 the numerical methods used to discretize the radiative transport and the diffusion equations and to perform the reconstructions. In Section 4, we present a quantitative comparison between transport-based and diffusion-based reconstructions. Conclusions are offered in Section 5.

2. Transport Equation and Its Diffusion Approximation

We introduce the two forward models for light propagation in tissues that are used in model-based optical tomographic reconstructions, namely, transport and diffusion models. To simplify the presentation, all the equations will be written in the frequency domain. The latter refers to the modulation frequency of the source term, typically on the order of 100–1000 MHz, and should not be confused with the frequency of the photons, which for near-infrared light lies between 300 and 500 THz and corresponds to wavelength of 600–1000 nm. The term "steady state," used later in the paper, refers to the case where the source modulation frequency (denoted by ω) equals zero.

A. Radiative Transport Equation

The propagation of near-infrared light in biological tissues is most accurately modeled by the RTE [1,37,38]. This equation describes the photon density in the phase space $X = \Omega \times S^2$, i.e., as a function of both position $\mathbf{x} \in \Omega \subset \mathbb{R}^3$ and propagation direction $\boldsymbol{\theta} \in S^2$. Here Ω is the spatial domain and S^2 the unit sphere in $\mathbb{R}^3$. When the intensity of the light source is modulated with frequency ω, i.e., is of the form $f(\mathbf{x}, \boldsymbol{\theta})e^{i\omega t}$, where t is the time variable, the frequency domain radiative transport equation takes the form [1,33,39]:

$$\left(\frac{i\omega}{\nu} + \boldsymbol{\theta}\cdot\nabla + \mu_t(\mathbf{x})\right)u(\mathbf{x},\boldsymbol{\theta}) - \mu_s(\mathbf{x}) \times \int_{S^2} k(\boldsymbol{\theta}\cdot\boldsymbol{\theta}')u(\mathbf{x},\boldsymbol{\theta}')\mathrm{d}\boldsymbol{\theta}' = 0, \quad \text{in } X,$$
$$u(\mathbf{x},\boldsymbol{\theta}) = f(\mathbf{x},\boldsymbol{\theta}), \qquad \text{on } \Gamma_-, \qquad (1)$$

where $i = \sqrt{-1}$ and ν is the speed of light in the medium. The functions $\mu_t(\mathbf{x})$ and $\mu_s(\mathbf{x})$ are the total absorption (extinction) coefficient and scattering coefficient, respectively. We denote by $\mu_a(\mathbf{x}) \equiv \mu_t(\mathbf{x}) - \mu_s(\mathbf{x})$ the physical absorption coefficient. The solution $u(\mathbf{x}, \boldsymbol{\theta})$ is the radiant power per unit solid angle per unit area perpendicular to the direction of propagation at $\mathbf{x}$ in the direction $\boldsymbol{\theta}$. The boundary sets $\Gamma_\pm$ are defined by

$$\Gamma_\pm = \{(\mathbf{x},\ \boldsymbol{\theta}) \in \partial\Omega \times S^2 \text{ such that } \pm\boldsymbol{\theta}\cdot\boldsymbol{v}(\mathbf{x}) > 0\}, \qquad (2)$$

with $\boldsymbol{v}(\mathbf{x})$ the outward unit normal to Ω at $\mathbf{x} \in \partial\Omega$. The scattering kernel for light propagation in tissues is highly forward peaked and is chosen in this paper as the Henyey–Greenstein phase function [40,41]:

$$k(\boldsymbol{\theta}\cdot\boldsymbol{\theta}') = C\,\frac{1-g^2}{(1+g^2-2g\cos\phi)^{3/2}} \equiv k(\phi), \qquad (3)$$

where ϕ is the angle between $\boldsymbol{\theta}$ and $\boldsymbol{\theta}'$, i.e., $\boldsymbol{\theta}\cdot\boldsymbol{\theta}' = \cos\phi$ and where $g \in [0, 1]$ is the anisotropy factor, which measures how forward peaked scattering is. The larger the value of g, the more forward peaked the scattering. The anisotropy factor is often used to define the so-called effective scattering coefficient through $\mu_s' = (1-g)\mu_s$. The normalization factor C is chosen such that $\int_{S^2} k(\boldsymbol{\theta}\cdot\boldsymbol{\theta}')\mathrm{d}\boldsymbol{\theta} = 1$. For scattering kernels other than Eq. (3), we refer interested readers to the reference cited [42].

We remark finally that both $f(\mathbf{x}, \boldsymbol{\theta})$ and $u(\mathbf{x}, \boldsymbol{\theta})$ depend also on the modulation frequency ω. For simplicity of notation, this dependency is not written explicitly.

B. Diffusion Approximation

The RTE we described is a microscopic model for light propagation in tissues. Numerical solutions of this model are very expensive because both spatial and angular discretizations have to be performed. It is thus preferable in many applications to replace the transport equation by the less expensive physical-space diffusion equation. The diffusion equation describes light propagation at the macroscopic level, where the unknown quantity is the angularly averaged photon flux.

The approximation of the radiative transport equation by the diffusion equation has been well-documented [43,44]. There, it is shown that when absorption is sufficiently low and scattering sufficiently large, the transport process can be modeled macroscopically with the following diffusion equation:

$$\frac{i\omega}{\nu}U(\mathbf{x}) - \nabla\cdot\mathcal{D}\nabla U + \mu_a(\mathbf{x})U(\mathbf{x}) = 0, \qquad \text{in } \Omega,$$
$$U + 3\epsilon L_3\boldsymbol{v}(\mathbf{x})\cdot\mathcal{D}\nabla U = \Lambda(f)(\mathbf{x}), \quad \text{on } \delta\Omega. \qquad (4)$$

Here $U(\mathbf{x})$ is the angularly averaged photon flux at $\mathbf{x}$, an approximation of the quantity $\int_{S^2} u(\mathbf{x}, \boldsymbol{\theta}')\mathrm{d}\boldsymbol{\theta}$ in the

transport equation; $\mu_a(\mathbf{x})$ is the absorption coefficient that describes the rate of absorption at $\mathbf{x}$. It corresponds to $\mu_t(\mathbf{x}) - \mu_s(\mathbf{x})$ in transport equation. The diffusion tensor $\mathcal{D}(\mathbf{x})$ is symmetric and positive definite. It is given by $\mathcal{D}(\mathbf{x}) = 1/(3(\mu_a(\mathbf{x}) + \mu_s'(\mathbf{x})))$ in the Henyey–Greenstein case, where $\mu_s'(\mathbf{x}) = (1 - g)\mu_s(\mathbf{x})$.

The operator Λ is a linear form that maps any incoming angular distribution f to a real number. Explicit expressions can be found in simple cases [43,45]. In this paper, we will always use isotropic source terms $f(\mathbf{x}, \boldsymbol{\theta}) = f(\mathbf{x})$ for which we obtain $\Lambda(f) = f$. This choice of f is not necessary in practice. It is picked here to simplify the comparison between transport and diffusion reconstructions.

A very important aspect in the derivation of diffusion equations is to account correctly for photon leakage at the domain boundary [26,43,46]. This requires a detailed boundary layer analysis for the transport equation [43], which shows that leakage should be modeled by the Robin-type boundary conditions for diffusion, where L_3 is the extrapolation length; see Eq. (4). Explicit expressions for the extrapolation length are known only in simple cases, for instance when scattering is isotropic ($g = 0$), where $L_3 \approx 0.7104$ [26,43,45].

The small parameter ϵ is called the transport mean free path. It is defined as $\epsilon = 3\mathcal{D} = 1/(\mu_a + \mu_s')$. The transport mean free path measures the average distance is takes for photons to be substantially deflected from their original direction by scattering. In the limit where the transport mean free path ϵ goes to zero, the error between the diffusion solution $U(\mathbf{x})$ and the transport flux $\int_{S^2} u(\mathbf{x}, \boldsymbol{\theta})\mathrm{d}\boldsymbol{\theta}$ is of order ϵ^2 in regions sufficiently far from the boundary [43].

In the time-dependent case, let us note that the diffusion approximation may not be valid for short times [43]. This implies that even in situations of highly scattering and low absorption, the diffusion approximation may not be accurate for high modulation frequencies ω. There is also numerical evidence for this statement [47].

3. Reconstruction Methods

Optical tomography aims at reconstructing $\mu_a(\mathbf{x})$ and $\mu_s(\mathbf{x})$ in the transport and diffusion equations from boundary measurements. Our goal here is to quantify the errors in the reconstructions obtained by using the diffusion equation in situations where it is not an accurate approximation to the RTE. To do this, we assume that the data are generated by the physically accurate transport model. We then consider two reconstructions.

1. Transport reconstruction. In this reconstruction, the radiative transport equation is used as the model for light propagation. The predicted current measurements at the domain boundary are then calculated using:

$$J_T(\mathbf{x}) = \int_{S_+^2} \boldsymbol{\theta} \cdot \boldsymbol{v}(\mathbf{x}) u(\mathbf{x}, \boldsymbol{\theta})\mathrm{d}\boldsymbol{\theta}, \tag{5}$$

where $S_+^2 = \{\boldsymbol{\theta}: \boldsymbol{\theta} \in S^2 \text{ and } \boldsymbol{\theta} \cdot \boldsymbol{v}(\mathbf{x}) > 0\}$.

2. Diffusion reconstruction. Here the diffusion equation is used as the light propagation model. The predicted boundary current measurements corresponding to Eq. (5) are computed according to

$$J_D(\mathbf{x}) = -\boldsymbol{v}(\mathbf{x}) \cdot \mathcal{D}\nabla U. \tag{6}$$

In this paper, we focus on the reconstruction of the absorption coefficient μ_a only and assume μ_s to be known. The reconstruction of μ_a is quite useful in many practical applications, such as, e.g., the monitoring of the oxygenation of tissues [19].

A. Reconstruction Algorithms

As usual, we solve the reconstruction problem by minimizing the mismatch between model predictions and measured data for several source-detector pairs:

$$\min_{\mu_a(\mathbf{x}) \in [\mu_a^{\min}, \mu_a^{\max}]} \mathcal{F}_\beta := \mathcal{F}(\mu_a) + \frac{\beta}{2}\int_\Omega \nabla\mu_a \cdot \nabla\mu_a \mathrm{d}\mathbf{x}, \tag{7}$$

where the last term is a Tikhonov regularization functional with regularization parameter β, and where the mismatch functional is defined as

$$\mathcal{F}(\mu_a(\mathbf{x})) \equiv \frac{1}{2}\sum_{q=1}^{N_q} \|J^q(\mathbf{x}) - z_q(\mathbf{x})\|^2_{L^2(\partial\Omega)}. \tag{8}$$

Here $\mu_a^{\min}$ and $\mu_a^{\max}$ are physical lower and upper bounds imposed on μ_a. N_q is the number of sources used, and $z_q(\mathbf{x})$ denotes the current measurements corresponding to source q. As stated before, we assume that the current data $z_q(\mathbf{x})$ are generated by the transport equation.

We use the limited memory Broyden–Fletcher–Goldfarb–Shanno (BFGS) algorithm that we have previously developed [33] to solve the minimization problem in Eq. (7). To use it for the diffusion case, we use the diffusion equation as the forward model and correspondingly modify the gradient calculations for the objective function. We adopt a very similar adjoint state method for the gradient calculation. We refer to our previous work [33] for details of the BFGS algorithm for the transport reconstructions and the L-curve method used to choose the regularization parameter β.

B. Discretization of Forward Models

To calculate model predictions for the minimization algorithm, we numerically solve the RTE in Eq. (1) by discretizing it using the discrete ordinate method for the angular variable and a finite volume method for

the spatial variable [33,39]. We refer to our earlier work [33,39] for some numerical tests on the finite volume discretization of the transport equation and related reconstruction results.

The diffusion Eq. (4) is discretized by using a similar finite volume method. Finite volume methods [48] ensure the conservation of mass (or momentum, energy) in a discrete sense, which is important in transport and diffusion calculations. They also have the advantage of easily handling complicated geometries by arbitrary triangulations, which we need in tomographic applications.

We denote by $\mathcal{M}$ a mesh of $\mathbb{R}^3$ consisting of polyhedral bounded convex subsets of $\mathbb{R}^3$. $\mathcal{M}$ covers our computational domain Ω. Let $\mathscr{C} \in \mathcal{M}$ be a *control cell*, that is, an element of the mesh $\mathcal{M}$, $\partial\mathscr{C}$ its boundary, and $V_{\mathscr{C}}$ its volume. We assume that the unknown quantity, for example $U(\mathbf{x})$, is constant in $\mathscr{C}$ and denote the value of $U(\mathbf{x})$ on $\mathscr{C}$ by $U^{\mathscr{C}}$.

Integrating the diffusion Eq. (4) over cell $\mathscr{C}$ and using the divergence theorem, we obtain the following equations:

$$-\int_{\partial\mathscr{C}} \mathbf{n}_{\mathscr{C}} \cdot \mathcal{D}\nabla U \mathrm{d}\gamma(\mathbf{x}) + \left(\mu_a{}^{\mathscr{C}} - \frac{i\omega}{\nu}\right) V_{\mathscr{C}} U^{\mathscr{C}} = 0, \quad (9)$$

where $\mathbf{n}_{\mathscr{C}}(\mathbf{x})$ denotes the outward normal to $\partial\mathscr{C}$ at point $\mathbf{x} \in \partial\mathscr{C}$, $\mathrm{d}\gamma(\mathbf{x})$ denotes the surface measure on $\partial\mathscr{C}$, and $\mu_a{}^{\mathscr{C}}$ is the value of μ_a on cell $\mathscr{C}$.

Now we have to approximate the flux through the boundary of $\mathscr{C}$, i.e., the first integral term in Eq. (9). Let $\{\mathscr{C}_i\}_{i=1}^{I}$ be the set of neighboring cells of $\mathscr{C}$. We denote by $S_{\mathscr{C},i}$ the common edge of cell $\mathscr{C}$ and $\mathscr{C}_i$, i.e., $S_{\mathscr{C},i} = \partial\mathscr{C} \cap \partial\mathscr{C}_i$. We then have

$$-\int_{\partial\mathscr{C}} \mathbf{n}_{\mathscr{C}}(\mathbf{x}) \cdot \mathcal{D}\nabla U \mathrm{d}\gamma(\mathbf{x}) = -\sum_i \int_{S_{\mathscr{C},i}} \mathbf{n}_{\mathscr{C}}(\mathbf{x}) \cdot \mathcal{D}\nabla U \mathrm{d}\gamma(\mathbf{x}). \quad (10)$$

The flux $\int_{S_{\mathscr{C},i}} \mathbf{n}_{\mathscr{C}}(\mathbf{x}) \cdot \mathcal{D}\nabla U \mathrm{d}\gamma(\mathbf{x})$ can be approximated by various numerical schemes. In this paper, we take a first-order scheme:

$$F^{\mathscr{C},i} := -\int_{S_{\mathscr{C},i}} \mathbf{n}_{\mathscr{C}}(\mathbf{x}) \cdot \mathcal{D}\nabla U \mathrm{d}\gamma(\mathbf{x}) = \frac{\mathcal{D}^{\mathbf{nn}} + \mathcal{D}_i{}^{\mathbf{nn}}}{2} |S_{\mathscr{C},i}| (U^{\mathscr{C}} - U^{\mathscr{C}_i})/\nabla, \quad (11)$$

where $|S_{\mathscr{C},i}|$ is the measure of $S_{\mathscr{C},i}$, Δ is the distance between the center of $\mathscr{C}$ and $\mathscr{C}_i$. The notation $\mathcal{D}^{\mathbf{nn}}$ denote the $\mathbf{nn}$ component of the diffusion tensor in the $(\boldsymbol{\tau}, \mathbf{n})$ coordinate system on surface $S_{\mathscr{C},i}$. In isotropic scattering case, it is just $\mathcal{D}$.

When $S_{\mathscr{C},i} \subset \partial\Omega$, we have

$$F^{\mathscr{C},i} := -\int_{S_{\mathscr{C},i}} \mathbf{n}_{\mathscr{C}}(\mathbf{x}) \cdot \mathcal{D}\nabla U \mathrm{d}\gamma(\mathbf{x}) = \frac{|S_{\mathscr{C},i}|}{nL_n}(U^{\mathscr{C}} - f). \quad (12)$$

We then obtain a full discretization of the diffusion equation:

$$\sum_i F^{\mathscr{C},i} + \left(\mu_a{}^{\mathscr{C}} - \frac{i\omega}{\nu}\right) V_{\mathscr{C}} U^{\mathscr{C}} = 0. \quad (13)$$

Let N denote the total number of control cells. After collecting the discretized diffusion Eq. (13) on all control cells, we arrive at the following system of complex-valued algebraic equations,

$$\mathbf{AU} = \mathbf{G}, \quad (14)$$

where $\mathbf{A} \in \mathbb{C}^{N\times N}$. The boundary source $\Lambda(f)(\mathbf{x})$, which comes into the discretized system via the flux approximation Eq. (11), is denoted by $\mathbf{G}$.

4. Numerical Results

We provide in this section several numerical experiments where we compare the reconstructions with diffusion and transport equations as the models for photon propagation.

A. Setup for the Reconstructions

For our numerical experiments we consider the three-dimensional cylindrical domain, $\Omega := \{(\mathbf{x}, z): |\mathbf{x}| < 1; 0 < z < 2\}$, with boundary $\partial\Omega := \{(\mathbf{x}, z): |\mathbf{x}| = 1; 0 < z < 2\} \cup \{(\mathbf{x}, z): |\mathbf{x}| < 1; z = 0\} \cup \{(\mathbf{x}, z): |\mathbf{x}| < 1; z = 2\}$. Here, for simplicity, we have used the notation $\mathbf{x} \equiv (x, y)$. We embed a small cylindrical inclusion,

$$\Omega_c = \{(\mathbf{x},\ z): |\mathbf{x} - (0.5,\ 0)| < 0.2,\ 0.2 < z < 1.8\},$$

into the domain. We show in Fig. 1 the XZ cross section of the domain at $y = 0$ and the XZ cross section at $z = 1$.

Four point sources are placed on the surface of the cylinder at $(-1, 0, 1)$, $(1, 0, 1)$, $(0, 1, 1)$, and $(0, -1, 1)$, respectively. All sources are isotropic such that we can use the same description in diffusion as in transport reconstructions. We place seven layers of

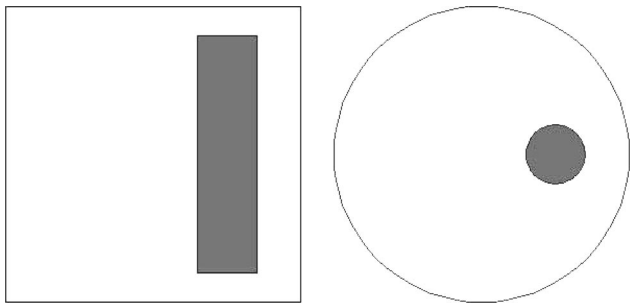

Fig. 1. XZ (at $y = 0$) and XY (at $z = 1$) cross sections of the computational domain.

detectors with z coordinate given by $z_i = i * 0.25$, $1 \leq i \leq 7$. On each layer, 32 detectors are uniformly distributed on the domain boundary. We partition the domain into 19,452 tetrahedral elements. A level symmetric discrete ordinate set [49] has been used to discretize the angular variable in the transport equation. A total number of 120 directions (corresponding to the discretization S_{10}) is used.

All synthetic data are generated with a discretization about twice as fine (in spatial variables) as the discretization used in the inversions to limit the so-called inverse crimes [50].

In Subsections 4.B–4.E, we consider reconstructions based on *noisy* data. Noise is added to the synthetic data in the following manner. Let $z_k \in \mathbb{C}$ be the kth exact data. We decompose it as $z_k = r_k e^{i\theta_k}$, with r_k a nonnegative real number. Then r_k and θ_k are corrupted by noise as $r_k^{\delta} = (1 + \delta * \text{rand}_{kr}) r_k$ and $\theta_k^{\delta} = (1 + \delta * \text{rand}_{k\theta})\theta_k$. Here, rand_{kr} and $\text{rand}_{k\theta}$ for all measurements $1 \leq k \leq K$ are independent identically distributed random variable on $(-1, 1)$ with uniform distribution (thus with variance $2/3$). The noisy kth data is then defined by $z_k^{\delta} = r_k^{\delta} e^{i\theta_k^{\delta}}$. Note that the same value of δ is chosen here to model noise on the phase and on the amplitude. This allows for a simpler presentation of the effects of noise on the reconstructions. Note also that noise is chosen multiplicative both on the phase and the intensity. Whereas multiplicative noise on the intensity is rather classical, our choice of multiplicative noise on the phase may be justified as follows. What is measured in practice is the phase shift with respect to the modulation of the source term. In the absence of scattering, photons thus accumulate a phase equal to $\omega l/c$, where l is the traveled distance from the source. In practical optical tomography with modulated sources, ω is at most 1 GHz so that $\omega/c \lesssim 3$. Since distances at on the order of a few centimeters, phase shifts $\omega l/c \lesssim 0.1$ in the absence of scattering are a fraction of π. The multiplicative noise on the phase thus implies that errors on the phase shift are larger on measurements away from the source, where phase shift is significant, than in the vicinity of the source, where it is close to 0.

The quality of the reconstructions is measured as follows. Denote by M^e and M^r the exact and reconstructed absorption coefficients, respectively. We then define the relative l^2 error between M^e and M^r by

$$\mathcal{E}_{l^2} = \frac{\|M^r - M^e\|_{l^2}}{\|M^e\|_{l^2}}. \tag{15}$$

B. Diffusive Media of Small Size

We compare reconstructions with diffusion and transport models in media of small size. Because the media are relatively small, the optical separation between the sources and the detectors is also relatively small. Photons undergo only a small number of scattering events between a source and a detector. It is well known that the diffusion approximation to the transport equation becomes less accurate in describing photon propagation when such small tissue volumes are considered. What we want to study in the section is how these inaccuracies affect the tomographic reconstructions in such media.

We consider the following setup. The background optical properties in the big cylinder is given by $\mu_a = 0.1\ \text{cm}^{-1}$, while $\mu_a = 0.2\ \text{cm}^{-1}$ for the inclusion, which is twice as high as the absorption coefficient of the background. We set the scattering coefficient $\mu_s = 100\ \text{cm}^{-1}$ for the whole domain. The anisotropic factor for the scattering kernel is $g = 0.9$ so that $\mu_s' = 10\ \text{cm}^{-1}$. The modulation frequency is set to $\omega = 0.0$ (steady state).

We show in Fig. 2 cross sections of the reconstructed absorption coefficient based on transport

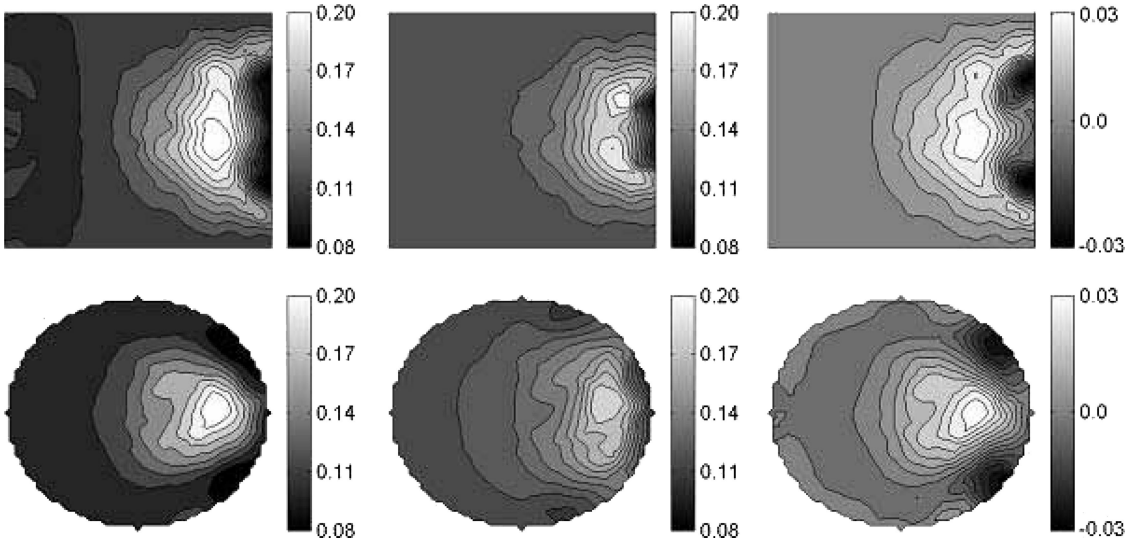

Fig. 2. Cross sections of the reconstructed absorption coefficients in domain of small size. Top row: XZ cross section at $y = 0$ for transport reconstruction (left), diffusion reconstruction (middle), and their difference (right). Bottom row: corresponding XY cross sections at $z = 1$. Reconstructions are done with noise-free data.

and diffusion equations with noise-free transport data. To stress the difference in the reconstruction, we also plot the difference of the reconstruction in Fig. 2.

We first observe that structures in the z direction are not well reconstructed in either case. This is because light sources are all located on the $z = 1$ plane. Few photons propagate sufficiently far along the z direction. We have verified that adding sources on other planes along the z axis makes the reconstructions better, as expected.

Our second observation is that the location of the inhomogeneity is found by both transport and diffusion reconstructions. However, the transport-based reconstruction provides a more accurate value of the actual optical properties of the inclusion. The diffusion reconstruction overestimates the volumes of the absorption coefficient in some places and underestimates the coefficients in the inclusion. This can be best seen on the right figures in Fig. 2 where we plot the difference between transport- and diffusion-based reconstructions.

Our numerical examples show that the difference between the transport and diffusion reconstructions becomes less prominent as noise contained in the measured data increases. This can be seen on the left in Fig. 3, where we plot the quantitative error in the reconstructions as a function of noise level. As noise level reaches a certain value, above 12% in this case, the difference between transport and diffusion reconstructions becomes almost indistinguishable.

We have performed a second group of simulations, where we increase the background scattering coefficient to $\mu_s = 150\ \mathrm{cm}^{-1}$ so that $\mu_s' = 15\ \mathrm{cm}^{-1}$. The reconstruction quality from noisy data is shown in Fig. 3. We see that although the medium is now 50% more diffusive, reconstructions based on the diffusion approximation do not significantly improve, because the domain still remains relatively thin optically. For typical values of the absorption and scattering parameters in tissues, the diffusion approximation is not very accurate in small domains such as fingers or small animals.

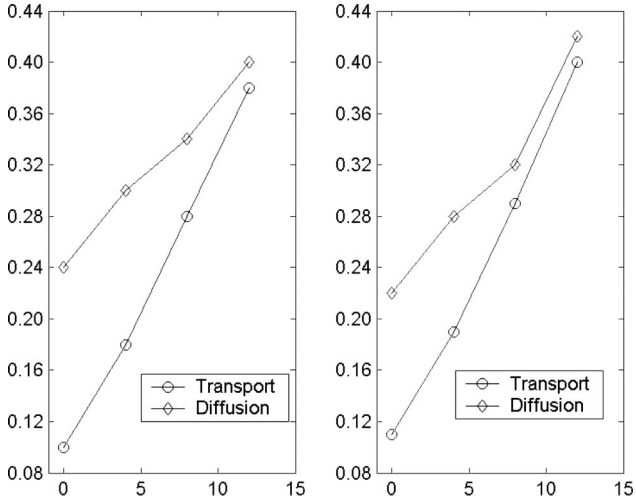

Fig. 3. Relative errors in transport and diffusion reconstructions using data with different noise levels (in percentage). Left: reconstructions with scattering coefficient $\mu_s = 100\ \mathrm{cm}^{-1}$; Right: reconstructions with scattering coefficient $\mu_s = 150\ \mathrm{cm}^{-1}$.

The last point we stress here is that transport-based reconstructions are computationally much more costly than diffusion-based reconstructions. Typically, we observe that diffusion reconstructions are about 60 times faster than transport reconstructions. Although the computational speed really depends on how one discretize the problem, we have observed in most cases an acceleration factor of at least 40 in diffusion reconstructions.

C. Effects of Modulation Frequency

As we have remarked before, in the frequency domain, the diffusion approximation works only for not-too-high modulation frequency [47]. Essentially, one has to scale the modulation frequency ω to ω/ϵ as one scale the absorption coefficient to derive the correct diffusion approximation in the limit of small mean free paths. This is similar to the scaling of the time variable in a time-dependent case [43]. In practice, however, relatively high modulation frequencies need to be used to obtain a significant phase shift that can be measured.

We consider here the same reconstructions as those of the last section though with measured data obtained at different modulation frequencies. We show in Fig. 4 reconstructions with modulation frequency of $\omega = 0.8$ GHz. Again we observe that the shape on the z direction is not well reconstructed in both cases. The location of the inhomogeneity is found by both the transport and the diffusion reconstructions.

As in Subsection 4.B, the transport-based reconstruction provides more accurate values of the actual optical properties of the inclusion. The differences of the two have been plotted on the right figures in Fig. 4.

As expected, the difference between diffusion- and transport-based results increases with the modulation frequency, as can be seen by comparing results in Figs. 4 and 2. This can also be seen from Fig. 5, where we plot the quality of reconstructions against the modulation frequency. Four modulation frequencies has been considered. They are 0.2, 0.4, 0.6, and 0.8 GHz. The quality of transport reconstructions slightly increases as the modulation frequency increases, but the quality of the diffusion reconstructions decreases as the modulation frequency increases.

As noise in the data increases, the difference between diffusion-based and transport-based reconstructions becomes smaller. We show in the right plot of Fig. 5 the quality of reconstructions with 12% multiplicative noise. Although there is still a difference between the two reconstructions (especially in the high frequency cases), the difference is much smaller than in the case of noise-free data.

Computationally, increasing the modulation frequency results in an increase of the computational time used to solve the inverse problem. This is due to

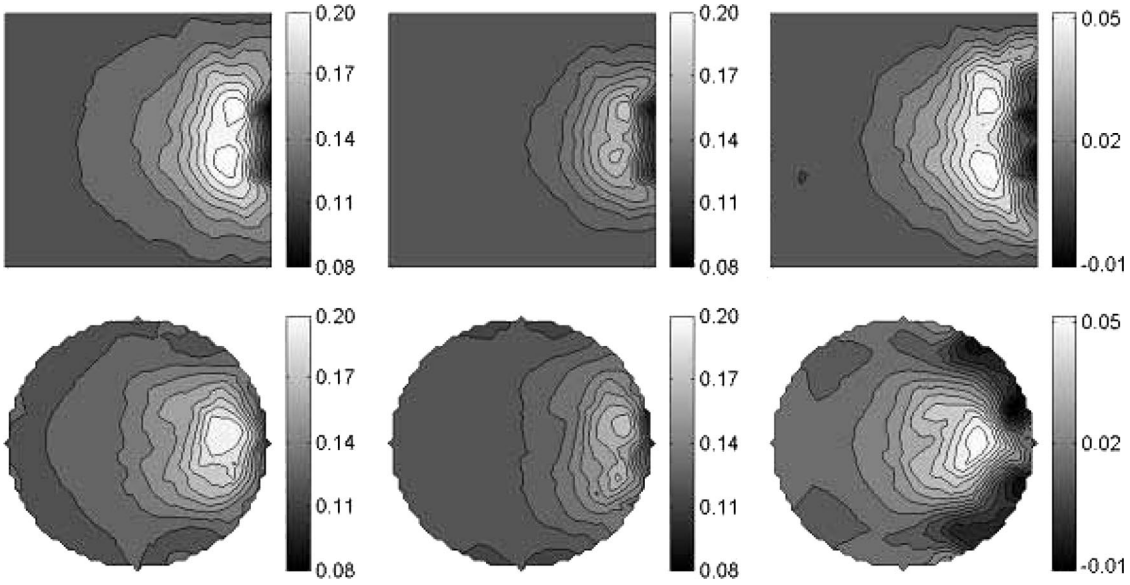

Fig. 4. Cross sections of reconstructed absorption coefficients with source of high modulation frequency. Top row: XZ cross section at $y = 0$ for transport reconstruction (left), diffusion reconstruction (middle), and their difference (right). Bottom row: corresponding XY cross sections at $z = 1$. The modulation frequency for the sources is $\omega = 0.8$ GHz.

the fact that modulation frequency appears on the off-diagonal elements of the matrices derived from the discretization of the equations. Increasing the frequency increases the condition number of the matrices. However, even in the high frequency situation, we still observe that transport-based reconstructions are about 50 times slower than diffusion-based reconstructions.

D. Impact of the Extrapolation Length

The choice of the extrapolation length in the diffusion equation has a significant influence on the solution of the diffusion equation, especially near the boundary [26,43]. We study in this section the effect of the extrapolation length on the quality of the reconstructions.

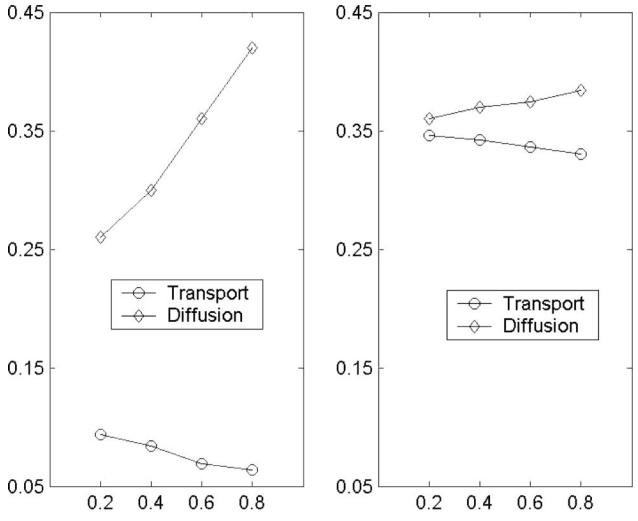

Fig. 5. Relative errors in reconstructions as functions of modulation frequencies (in gigahertz). Left; reconstructions with noise-free data; right: reconstructions with 12% noise in the data.

All simulations in this section are done with isotropic scattering. In other words, we have set the anisotropic factor to $g = 0$. The scattering coefficient is set to be $\mu_s = 10\ \mathrm{cm}^{-1}$. We show in Fig. 6 the reconstructions using the transport equation and diffusion equation with extrapolation length $L_3 = 0$. The data here are noise free.

We see from Fig. 6 that there is a significant amount of overshooting in the diffusion reconstructions. The quality of the diffusion-based reconstruction also decreases when very large extrapolation lengths are used. In Fig. 7 we compare the quality of reconstructions by diffusion equations with various extrapolation lengths. Although the least difference between diffusion and transport reconstructions may not happen exactly at the place of right extrapolation length, it does happen when a value close to the right value is chosen. We thus conclude that that extrapolation length does have a significant impact on the quality of reconstructions.

As usual, noise in the data plays a significant role. The difference between transport-based and diffusion-based is already very small when the noise level reaches 12%. One would expect that as noise increases, the difference would become indistinguishable again. Computationally, we observe that transport-based reconstructions are still $\sim$50 times slower than diffusion-based reconstructions again.

E. Diffusive Media with Void Regions

The last case we want to discuss is the situation when nonscattering void regions are present in the domain. It has been shown in various situations that when void region presents in scattering media, diffusion

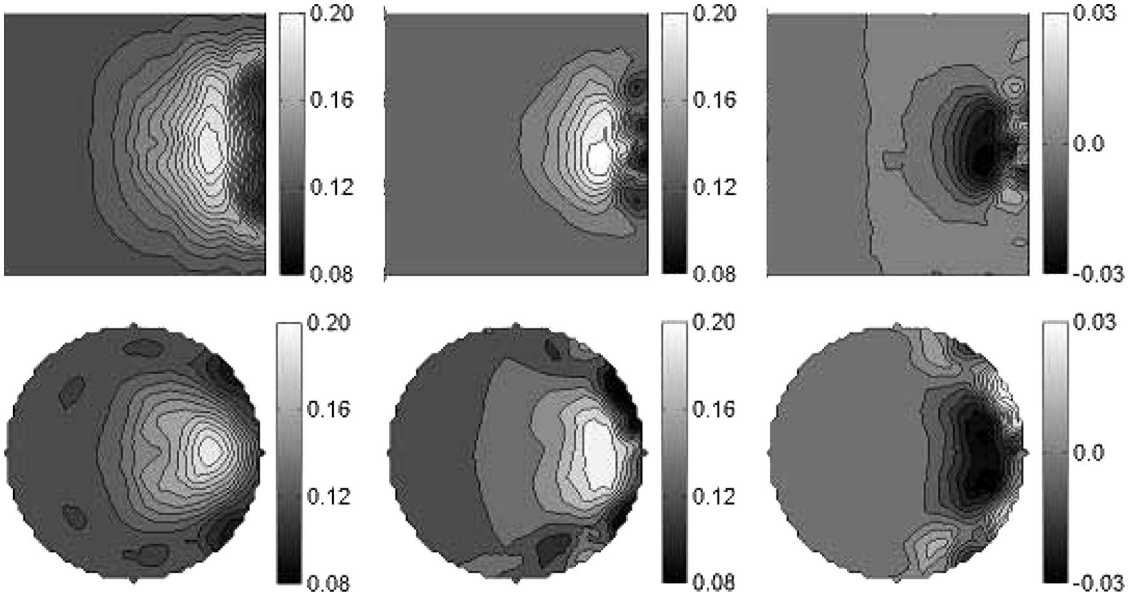

Fig. 6. Cross sections of reconstructed absorption coefficients with zero extrapolation length. Top row: *XZ* cross section at $y = 0$ for transport reconstruction (left), diffusion reconstruction (middle), and their difference (right). Bottom row: corresponding *XY* cross sections at $z = 1$. Reconstructions are done with noise-free data.

equations fail to approximate transport accurately [25,26,37]. Special attention has to be paid when using diffusion equations in this situation.

We again consider here the reconstruction of the absorption coefficient in the cylinder and assume that $\mu_s(\mathbf{x})$ is known. We embed a void cylindrical inclusion centered at $(-0.5, 0)$ in the media. It is of the same size as the absorbing inclusion; see Fig. 8 for the geometrical setting. Void means that the scattering and absorption coefficients vanish in that region. As in Subsection 4.D we set the scattering coefficient $\mu_s = 10\ \mathrm{cm}^{-1}$, and anisotropy factor $g = 0$ in the rest of the domain. In the diffusion equation, we replace the diffusion coefficient in the void region by its surrounding diffusion coefficient. In the absence of a better guess, this is better than evaluating the diffusion coefficient $\mathcal{D} = 1/(3\mu_t)$ as being infinite, though better choices yet may be available [25,51].

We show in Fig. 9 results from reconstructions with noise-free data. The transport reconstruction looks quite similar to the one in Fig. 2. The diffusion reconstruction however, looks very different. The diffusion model generates spurious absorption at the location of the void to compensate for the wrong transport of photons in that area. Whereas voids have little effect on the absorption reconstruction with the transport model (provided that we know where the void is), they further degrade diffusion reconstructions unless the void region is modeled appropriately [25,28,51–53].

The transport and diffusion reconstructions in the presence of a void have been performed with different noise levels in the measured data. The quality of the reconstructions is plotted against the noise level in Fig. 10. As noise increases, the difference between transport and diffusion equations decreases. One can

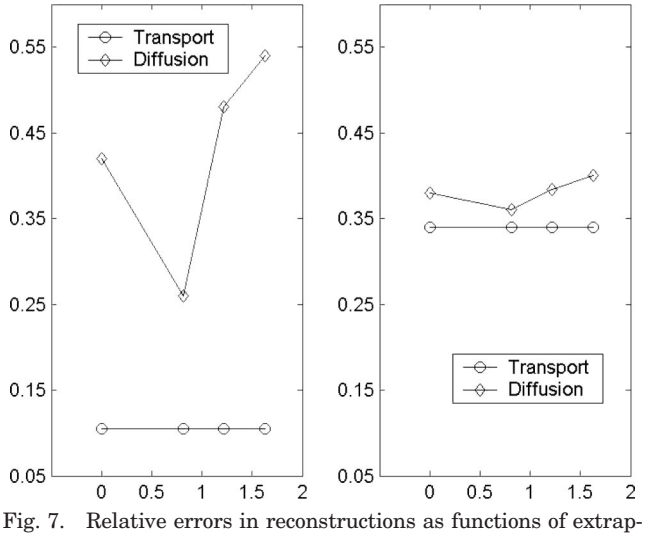

Fig. 7. Relative errors in reconstructions as functions of extrapolation length. Left: reconstructions with noise-free data; Right: reconstructions with 12% noise in the data. Transport reconstructions are shown here just as a reference.

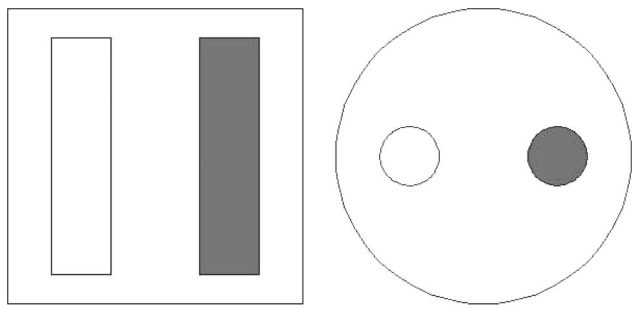

Fig. 8. *XZ* ($y = 0$) and *XY* ($z = 1$) cross sections of the computational domain with a void inclusion.

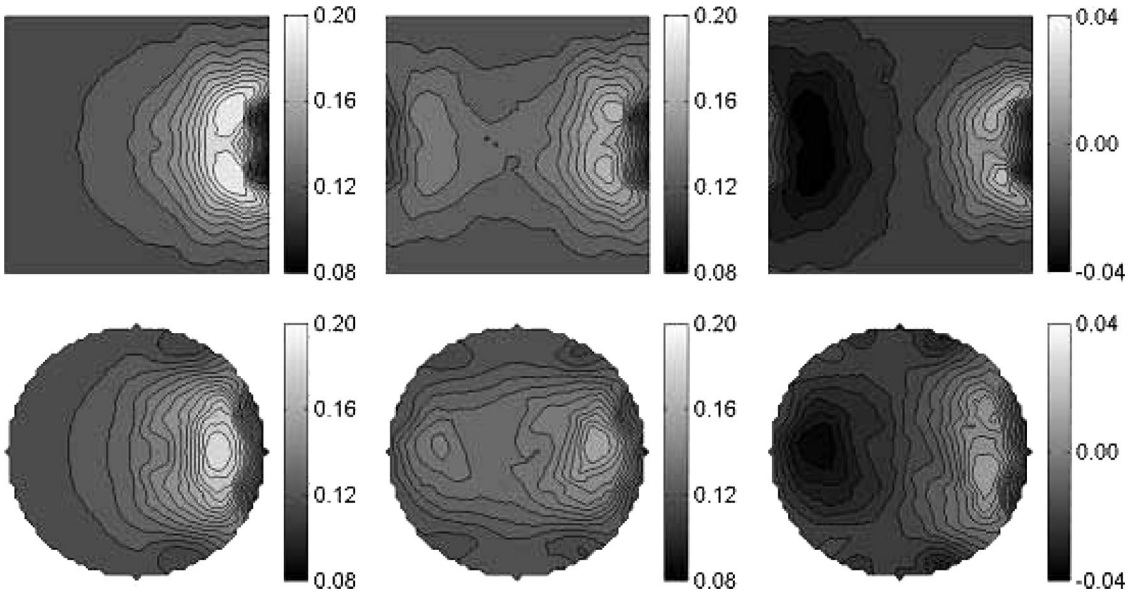

Fig. 9. Cross sections of reconstructed absorption coefficients in media with void regions. Top row: *XZ* cross section at $y = 0$ for transport reconstruction (left), diffusion reconstruction (middle), and their difference (right). Bottom row: corresponding *XY* cross sections at $z = 1$. A void region is embedded in the domain.

expect that when the noise in the data reaches a certain level, here about 12% of multiplicative noise, the difference between the transport and diffusion reconstructions may become indistinguishable. Similar results for reconstructions with a background scattering coefficient $\mu_s = 15\ \mathrm{cm}^{-1}$ are shown in the right panel of Fig. 10.

From the point of view of computational cost, the transport-based reconstructions become slightly faster here because of the presence of the void region. But it is far from being comparable to diffusion reconstructions. We still observe that transport-based reconstructions are about 40 times slower than diffusion-based reconstructions.

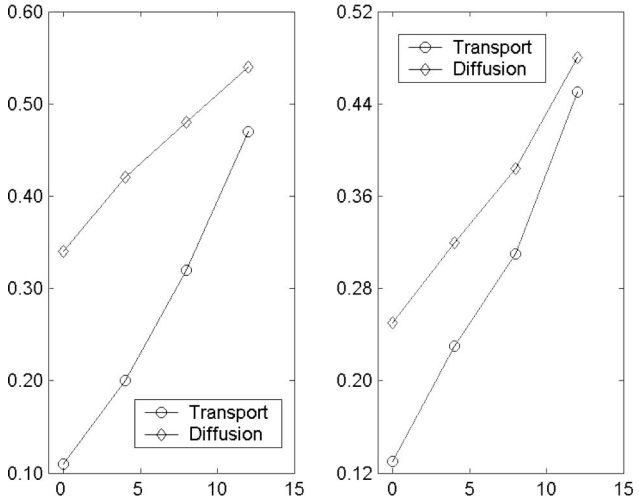

Fig. 10. Relative errors in transport and diffusion reconstructions using data with different noise levels in the presence of a void. Left: reconstructions with scattering coefficient $\mu_s = 10\ \mathrm{cm}^{-1}$; Right: reconstructions with scattering coefficient $\mu_s = 15\ \mathrm{cm}^{-1}$. Anisotropy factor $g = 0$ in both cases.

5. Conclusions and Remarks

We have conducted a comparative study of optical tomographic reconstructions based on transport and diffusion models in media of small (optical) volume. Small volume is of particular interest in applications such as imaging of joint diseases in human fingers [20–24] and monitoring of brain activity and tumor growth in small animals [34–36]. We have shown that diffusion-based reconstructions of absolute optical properties were significantly less accurate in such geometries. Although both the diffusion and transport reconstructions are usually able to locate an inhomogeneity buried in the media, transport-based reconstructions provide more accurate values of the absolute optical properties, in this paper the absorption, of inclusions.

We have quantified the role on the reconstruction of such factors as the source modulation frequency, the extrapolation length used in the diffusion model, and the presence of void regions. Whereas increasing the source modulation frequency improves transport solutions, it usually degrades the diffusion solutions. We have seen that poorly modeled void inclusions in the diffusion model generated spurious absorbing inclusions at the void location. In each situation, we have quantified the errors made by the transport and diffusion reconstructions.

We have characterized the effects of noise in the measured data. When multiplicative noise reaches a certain level, about 12% in our simulations, the transport and diffusion reconstructions becomes almost indistinguishable. However, given that a state-of-the-art optical imaging system shows noise levels of typically

less than 5% or even 1%, the benefits of transport-based reconstructions can be realized with most of the currently available systems [16,19,20,36,54]. Of course, the difference between diffusion- and transport-based reconstruction can be also be indistinguishable if the contract of the absorption coefficient of the background and the inclusions is too small.

Computationally, however, the diffusion-based reconstructions are favorable. In the examples considered here, we have consistently observed that transport-based reconstructions were ~50 times times more expensive than diffusion-based reconstructions.

We conclude this paper by stressing that we do not consider the case when time-dependent measurements can be used. In that case, the numbers we obtained here might need to be changed. We also noticed that other techniques such as using spectral difference measurements may also extend the applicability of the diffusion approximation to some cases considered here [55,56]. For example Pei *et al.* showed that relative changes in optical properties, which were obtained from relative measurement data (e.g., before and after pressure cuffs on an arm, or before and after certain brain stimulations, or differences in spectral measurements), could be reconstructed with high accuracy compared to absolute values using a diffusion-based code [56]. Testing if the same holds true for transport-based codes is beyond the scope of this paper, but should be addressed in future studies.

We would like to thank the anonymous referees for their valuable comments that helped us to improve the quality of this paper. The work of K. Ren and A. H. Hielscher was supported in part by the National Institute of Biomedical Imaging and Bioengineering (grant 5R01EB001900) and the National Institute of Arthritis and Musculoskeletal and Skin Diseases (grant 5R01AR046255), which are divisions of the National Institutes of Health. G. Bal also acknowledges support from the National Science Foundation (grant DMS-0239097) and an Alfred P. Sloan Fellowship.

References

1. S. R. Arridge, "Optical tomography in medical imaging," Inverse Probl. **15,** R41–R93 (1999).
2. D. A. Boas, D. H. Brooks, E. L. Miller, C. A. DiMarzio, M. Kilmer, R. J. Gaudette, and Q. Zhang, "Imaging the body with diffuse optical tomography," IEEE Signal Process Mag. **18,** 57–75 (2001).
3. B. Chance, R. R. Alfano, B. J. Tromberg, and A. Katzir, eds., in *Optical Tomography and Spectroscopy of Tissue* (SPIE, 2003), Vol. V.
4. E. M. C. Hillman, J. C. Hebden, M. Schweiger, H. Dehghani, F. E. W. Schmidt, D. T. Delpy, and S. R. Arridge, "Time resolved optical tomography of the human forearm," Phys. Med. Biol. **46,** 1117–1130 (2001).
5. H. Jiang, K. D. Paulsen, U. L. Österberg, B. W. Pogue, and M. S. Patterson, "Simultaneous reconstruction of optical absorption and scattering maps turbid media from near-infrared frequency-domain data," Opt. Lett. **20,** 2128–2130 (1995).
6. A. Li, E. Miller, M. Kilmer, T. Brukilacchio, T. Chaves, J. Stott, Q. Zhang, T. Wu, M. Chorlton, R. Moore, D. Kopans, and D. Boas, "Tomographic optical breast imaging guided by three-dimensional mammography," Appl. Opt. **42,** 5181–5190 (2003).
7. V. A. Markel and J. C. Schotland, "Inverse problem in optical diffusion tomography. 1. Fourier–Laplace inverse formula," J. Opt. Soc. Am. A **18,** 1336–1347 (2001).
8. V. A. Markel and J. C. Schotland, "Inverse problem in optical diffusion tomography. 2. Role of boundary conditions," J. Opt. Soc. Am. A **19,** 558–566 (2002).
9. G. J. Müller, ed., *Medical Optical Tomography: Functional Imaging and Optical Technologies* (SPIE, 1993), Vol. IS11.
10. B. W. Pogue, M. S. Patterson, H. Jiang, and K. D. Paulsen, "Initial assessment of a simple system for frequency domain diffuse optical tomography," Phys. Med. Biol. **40,** 1709–1729 (1995).
11. R. Roy and E. M. Sevick–Muraca, "Truncated Newton's optimization scheme for absorption and fluorescence optical tomography (part 1 and part 2)," Opt. Express **4,** 353–382 (1999).
12. M. Schweiger, S. Arridge, and D. Delpy, "Application of the finite-element method for the forward and inverse models in optical tomography," J. Math. Imaging Vision **3,** 263–283 (1993).
13. A. G. Yodh and B. Chance, "Spectroscopy and imaging with diffusing light," Phys. Today **48,** 34–40 (1995).
14. D. A. Benaron, S. R. Hintz, A. Villringer, D. Boas, A. Kleinschmidt, J. Frahm, C. Hirth, H. Obrig, J. C. van Houten, E. L. Kermit, W. F. Cheong, and D. K. Stevenson, "Noninvasive functional imaging of human brain using light," J. Cereb. Blood Flow Metab. **20,** 469–477 (2000).
15. D. A. Boas, K. Chen, D. Grebert, and M. A. Franceschini, "Improving the diffuse optical imaging spatial resolution of the cerebral hemodynamic response to brain activation in humans," Opt. Lett. **29,** 1506–1508 (2004).
16. B. W. Pogue, S. P. Poplack, T. O. McBride, W. A. Wells, K. S. Osterman, U. L. Osterberg, and K. D. Paulsen, "Quantitative hemoglobin tomography with diffuse near-infrared spectroscopy: pilot results in the breast," Radiology **218,** 261–266 (2001).
17. B. W. Pogue, M. Testorf, T. O. McBride, U. L. Österberg, and K. D. Paulsen, "Instrumentation and design of frequency-domain diffuse optical imager for breast cancer detection," Opt. Express **1,** 391–403 (1997).
18. P. Taroni, G. Danesini, A. Torricelli, A. Pifferi, L. Spinelli, and R. Cubeddu, "Clinical trial of time-resolved scanning optical mammography at 4 wavelengths between 683 and 975 nm," J. Biomed. Opt. **9,** 464–473 (2004).
19. B. J. Tromberg, N. Shah, R. Lanning, A. Cerussi, J. Espinoza, T. Pham, L. Svaasand, and J. Butler, "Noninvasive *in vivo* characterization of breast tumors using photon migration spectroscopy," Neoplasia **2,** 26–40 (2000).
20. A. H. Hielscher, A. D. Klose, A. Scheel, B. Moa–Anderson, M. Backhaus, U. Netz, and J. Beuthan, "Sagittal laser optical tomography for imaging of rheumatoid finger joints," Phys. Med. Biol. **49,** 1147–1163 (2004).
21. A. D. Klose, A. H. Hielscher, K. M. Hanson, and J. Beuthan, "Three-dimensional optical tomography of a finger joint model for diagnostic of rheumatoid arthritis," Proc. SPIE **3566,** 151–160 (1998).
22. U. Netz, J. Beuthan, H. J. Capius, H. C. Koch, A. D. Klose, and A. H. Hielscher, "Imaging of rheumatoid arthritis in finger joints by sagittal optical tomography," Medical Laser Application **16,** 306–310 (2001).
23. V. Prapavat, W. Runge, J. Mans, A. Krause, J. Beuthan, and G. Müller, "Development of a finger joint phantom for the optical simulation of early stages of rheumatoid arthritis," Biomed. Tech. **42,** 319–326 (1997).
24. Y. Xu, N. Iftimia, H. Jiang, L. Key, and M. Bolster, "Three-dimensional diffuse optical tomography of bones and joints," J. Biomed. Opt. **7,** 88–92 (2002).

25. G. Bal and K. Ren, "Generalized diffusion model in optical tomography with clear layers," J. Opt. Soc. Am. A **20,** 2355–2364 (2003).
26. G. Bal, "Particle transport through scattering regions with clear layers and inclusions," J. Comp. Physiol. **180,** 659–685 (2002).
27. G. Bal and Y. Maday, "Coupling of transport and diffusion models in linear transport theory," Math. Modell. Numer. Anal. **36,** 69–86 (2002).
28. H. Dehghani, S. R. Arridge, M. Schweiger, and D. T. Delpy, "Optical tomography in the presence of void regions," J. Opt. Soc. Am. A **17,** 1659–1670 (2000).
29. G. S. Abdoulaev and A. H. Hielscher, "Three-dimensional optical tomography with the equation of radiative transfer," J. Electron. Imaging **12,** 594–601 (2003).
30. W. Cai, M. Xu, and R. R. Alfano, "Three-dimensional radiative transfer tomography for turbid media," IEEE J. Sel. Top. Quantum Electron. **9,** 189–198 (2003).
31. O. Dorn, "A transport-backtransport method for optical tomography," Inverse Probl. Eng. **14,** 1107–1130 (1998).
32. A. D. Klose and A. H. Hielscher, "Optical tomography using the time-independent equation of radiative transfer. 2. inverse model," J. Quant. Spectrosc. Radiat. Transf. **72,** 715–202 (2002).
33. K. Ren, G. Bal, and A. H. Hielscher, "Frequency domain optical tomography based on the equation of radiative transfer," SIAM J. Sci. Comput. (USA) **28,** 1463–1489 (2006).
34. A. Y. Bluestone, M. Stewart, B. Lei, I. S. Kass, J. Lasker, G. S. Abdoulaev, and A. H. Hielscher, "Three-dimensional optical tomographic brain imaging in small animals, part 1: Hypercapnia," J. Biomed. Opt. **9,** 1046–1062 (2004).
35. E. E. Graves, R. Weissleder, and V. Ntziachristos, "Fluorescence molecular imaging of small animal tumor models," Current Molecular Medicine **4,** 419–430 (2004).
36. A. H. Hielscher, "Optical tomographic imaging of small animals," Curr. Opi. Biotechnol. **16,** 79–88 (2005).
37. A. H. Hielscher, R. E. Alcouffe, and R. L. Barbour, "Comparison of finite-difference transport and diffusion calculations for photon migration in homogeneous and heterogeneous tissue," Phys. Med. Biol. **43,** 1285–1302 (1998).
38. A. D. Kim and J. B. Keller, "Light propagation in biological tissue," J. Opt. Soc. Am. A **20,** 92–98 (2003).
39. K. Ren, G. S. Abdoulaev, G. Bal, and Andreas H. Hielscher, "Algorithm for solving the equation of radiative transfer in the frequency domain," Opt. Lett. **29,** 578–580 (2004).
40. L. G. Henvey and J. L. Greenstein, "Diffuse radiation in the galaxy," Astrophys. J. **90,** 70–83 (1941).
41. A. J. Welch and M. J. C. Van–Gemert, *Optical-Thermal Response of Laser Irradiated Tissue* (Plenum, 1995).
42. A. Kienle, F. K. Forster, and R. Hibst, "Influence of the phase function on determination of the optical properties of biological tissue by spatially resolved reflectance," Opt. Lett. **26,** 1571–1573 (2001).
43. R. Dautray and J.-L. Lions, *Mathematical Analysis and Numerical Methods for Science and Technology* (Springer–Verlag, 1993), Vol. 6.
44. R. Elaloufi, R. Carminati, and J. Greffet, "Time-dependent transport through scattering media: from radiative transfer to diffusion," J. Opt. A, Pure Appl. Opt. **4,** S103–S108 (2002).
45. S. Chandrasekhar, *Radiative Transfer* (Dover, 1960).
46. R. C. Haskell, L. O. Svaasand, T.-T. Tsay, T.-C. Feng, M. S. McAdams, and B. J. Tromberg, "Boundary conditions for the diffusion equation in radiative transfer," J. Opt. Soc. Am. A **11,** 2727–2741 (1994).
47. M. Francocur, R. Vaillon, and D. R. Rousse, "Theoretical analysis of frequency and time-domain methods for optical characterization of absorbing and scattering media," J. Quant. Spectrosc. Radiat. Transf. **93,** 139–150 (2005).
48. R. Eymard, T. Gallouet, and R. Herbin, "Finite volume methods," in *Handbook of Numerical Analysis VII,* P. G. Ciarlet and J. L. Lions, ed. (North–Holland, 2000).
49. E. E. Lewis and W. F. Miller, *Computational Methods of Neutron Transport* (American Nuclear Society, 1993).
50. D. Colton and R. Kress, *Inverse Acoustic and Electromagnetic Scattering Theory* (Springer–Verlag, 1998).
51. G. Bal, "Transport through diffusive and nondiffusive regions, embedded objects, and clear layers," SIAM J. Appl. Math. **62,** 1677–1697 (2002).
52. S. R. Arridge, H. Dehghani, M. Schweiger, and E. Okada, "The finite element model for the propagation of light in scattering media: a direct method for domains with nonscattering regions," Med. Phys. **27,** 252–264 (2000).
53. M. Firbank, S. R. Arridge, M. Schweiger, and D. T. Delpy, "An investigation of light transport through scattering bodies with nonscattering regions," Phys. Med. Biol. **41,** 767–783 (1996).
54. C. H. Schmitz, M. Löcker, J. M. Lasker, A. H. Hielscher, and R. L. Barbour, "Instrumentation for fast functional optical tomography," Rev. Sci. Instrum. **73,** 429–439 (2002).
55. H. Xu, B. W. Pogue, R. Springett, and H. Dehghani, "Spectral derivative based image reconstruction provides inherent insensitivity to coupling and geometric errors," Opt. Lett. **30,** 2912–2914 (2005).
56. Y. Pei, H. L. Graber, and R. L. Barbour, "Influence of systematic errors in reference states on image quality and on stability of derived information for DC optical imaging," Appl. Opt. **40,** 5755–5769 (2001).